Nanoscale

PAPER

Cite this: *Nanoscale*, 2016, **8**, 8008

Directional fluorescence emission co-enhanced by localized and propagating surface plasmons for biosensing†

Yi Wang,*[a,e] Lin Wu,[b] Ten It Wong,[c] Martin Bauch,[d] Qingwen Zhang,[e] Jinling Zhang,[a] Xiaohu Liu,[a] Xiaodong Zhou,[c] Ping Bai,[b] Jakub Dostalek*[d] and Bo Liedberg*[a]

Received 11th December 2015,
Accepted 8th March 2016

DOI: 10.1039/c5nr08816j

www.rsc.org/nanoscale

We investigated the simultaneous excitation of localized surface plasmons (LSPs) and propagating surface plasmons (PSPs) on a thin metallic film with an array of nanoholes for the enhancement of fluorescence intensity in heterogeneous bioassays. Experiments supported by simulations reveal that the co-excitation of PSP and LSP modes on the nanohole array in a Kretschmann configuration allows for fluorescence enhancement of about 10^2 as compared to a flat Au surface irradiated off-resonance. Moreover, this fluorescence signal was about 3-fold higher on the substrate supporting both PSPs and LSPs than that on a flat surface where only PSPs were resonantly excited. Simulations also indicated the highly directional fluorescence emission as well as the high fluorescence collection efficiency on the nanohole array substrate. Our contribution attempts to de-convolute the origin of this enhancement and identify further ways to maximize the efficiency of surface plasmon-enhanced fluorescence spectroscopy for implementation in ultra-sensitive bioassays.

Introduction

Surface plasmons (SPs) are optical resonances originating from excitation of free electron oscillations at the surface of metals. They allow for strong electromagnetic field confinement in the vicinity of such surfaces and have found diverse applications in analytical technologies,[1,2] photo-catalysis,[3–6] and opto-electronic devices.[7–10] Besides enabling direct detection of molecular binding events by measuring induced local refractive index changes, plasmonic nanostructures featuring strong enhancement of the electric field intensity offer powerful means for amplifying spectroscopic signals in surface-enhanced Raman scattering (SERS)[11,12] and metal enhanced fluorescence (MEF).[13–15] The fluorescence emission from emitters such as organic dyes or quantum dots can be enhanced by coupling their excitation (at wavelength λ_{ab} close to the absorption band) or emission (at emission wavelength λ_{em}) transitions with SPs. The SP-driven excitation at λ_{ab} allows for local enhancement of the excitation rate without increasing the background while the SP-mediated emission can be used to control the angular distribution of emitted light. Highly directional fluorescence emission[16,17] was demonstrated for the out-coupling of fluorescence light emitted *via* propagating surface plasmons (PSPs)[18,19] by a reverse Kretschmann configuration as well as for the emission mediated by localized surface plasmons (LSPs) supported by plasmonic nanoantennas.[20–23] Up to now, various metallic (nano)structures have been employed for the enhancement of fluorescence emission by combined coupling of emitter absorption and emission with SPs including continuous thin metallic films supporting PSPs,[13] and metallic nanostructures such as nanocubes,[24] nanoholes,[25–28] nanorods,[29,30] nanodisks,[31] core–shell nanoparticles,[32,33] DNA-assembled nanoparticles,[34] antennas-in-box[35] and bowtie nanoantennas[36] that support LSPs.[37] The amplified fluorescence signals have been implemented in various bioassays for highly sensitive detection of proteins and nucleic acid analytes[38,39] with limits of detection (LODs) reaching femtomolar concentration levels. In general, plasmon-enhanced fluorescence biosensors can provide sensitivity that is up to 4 to 5 orders of magnitude better than classical label-

[a]*Centre for Biomimetic Sensor Science, School of Materials Science and Engineering, Nanyang Technological University, 50 Nanyang Drive, Singapore 637553. E-mail: bliedberg@ntu.edu.sg*
[b]*Electronics and Photonics Department, Institute of High Performance Computing, Agency for Science, Technology, and Research (A*STAR), 1 Fusionopolis Way, Singapore 138632*
[c]*Institute of Materials Research and Engineering, Agency for Science, Technology and Research (A*STAR), 3 Research Link, Singapore 117602*
[d]*Biosensor Technologies, AIT-Austrian Institute of Technology GmbH, Muthgasse 11, 1190 Vienna, Austria. E-mail: Jakub.dostalek@ait.ac.at*
[e]*Wenzhou Institute of Biomaterials and Engineering, Chinese Academy of Sciences, Wenzhou, 325001 China. E-mail: wangyi@wibe.ac.cn*
† Electronic supplementary information (ESI) available: Details of nanostructure design, AFM and calculation of molecular coverage. See DOI: 10.1039/c5nr08816j

free surface plasmon resonance (SPR) biosensors and 1 to 2 orders of magnitude better than ELISA.[40]

Optical excitation of PSPs in the red and near infrared part of the spectrum at the surface of noble metals such as gold and silver provides electric field intensity enhancement $|E/E_0|^2$ of ~10–10^2 due to the field confinement in the direction perpendicular to the surface. This confinement can be quantified by the penetration depth L_p (defined as a distance from the metal surface where the surface plasmon electric field amplitude drops by a factor of $1/e$) which for PSP equals ~10^2 nm. The field intensity can be further enhanced by engineering PSP modes in order to decrease their Ohmic loss (*e.g.* long range surface plasmons[40–43]) which translates into an enhancement of fluorescence light intensity by a factor up to EF ~ 10^2. Another efficient means to confine the light intensity and amplify the fluorescence signal can be utilized by LSPs that exhibit stronger confinement of the electromagnetic field at distances L_p smaller than a few tens of nanometers. The tighter field confinement of LSPs has been utilized for the amplification of fluorescence intensity which can reach an enhancement factor of EF > 10^2 for surface-averaged and even >10^3 for individual emitters placed directly at a plasmonic "hot spot".[36] It should be noted that a plasmonic hot spot refers to a small volume at which metallic nanostructures confine the electromagnetic field by resonant excitation of LSPs.

In heterogeneous plasmon-enhanced fluorescence bioassays, the surface of metallic (nano)structures is functionalized with a biomolecular recognition element (*e.g.*, antibody) that specifically bind the target analyte of interest. Typically, the captured analyte is subsequently reacted with another molecule (*e.g.*, detection antibody) that is labelled with a fluorescence emitter (*e.g.* organic dye, quantum dot). The analyte binding events are detected by monitoring the fluorescence intensity emitted upon probing with the confined SP field. Probing by LSPs can lead to a substantial enhancement of the fluorescence signal. The enhancement is typically limited by the distribution of the plasmonic hot spots that occupy just a small fraction of the sensing spot area. Therefore, the probability of capturing the analyte at the hot spots is low which severely impedes the overall assay sensitivity.

In this paper, the simultaneous excitation of LSP and PSP modes on a Au film with an array of nanoholes is investigated for the amplification of fluorescence emission by combining the advantages of LSPs (increased field confinement at hot spots) and PSPs (large surface area that is probed by the SP field). Similar structures have been studied for other modalities of plasmonic biosensors. For instance, Au nanohole arrays integrated with nanocone arrays have shown strong field enhancement through coupling of LSPs.[44] Nanoporous metallic films supporting LSPs and PSPs have been used to study molecular binding events.[45] Similarly, silver nanowell substrates that were prepared from an anodized aluminum oxide template enabled simultaneous excitation of LSP and PSP, in which the PSP was expected to collect the energy of the incident light and re-excite LSP for SERS enhancement.[46] In addition, the coupling of LSP on Au nanoparticles with PSP on the Au film was explored for increasing the field intensity in the gaps between a nanoparticle and a metal surface. This approach was reported to provide SERS enhancement up to 10^7,[47] and a fluorescence enhancement yield up to EF ~ 10^3.[48] Furthermore, dye molecules placed in a small gap between a silver nanocube and a Au film provides highly directional fluorescence emission.[24] However, the use of these approaches for practical applications is limited by the size of the gap. It has to be rather narrow (typically 3–5 nm) which does not allow for accommodating larger molecules such as antibodies and cannot be used for regular assays. We herein investigate fluorescence emission mediated by co-excitation of LSP and PSP modes on Au nanohole arrays in order to tailor it for the amplification in fluorescence bioassays.

Experimental

Materials

Triethylene glycol mono-11-mercaptoundecylether (thiol-PEG, #673110), PBS buffer tablets, and Tween-20 were purchased from Sigma-Aldrich (Singapore). Biotinylated PEG alkane thiol (thiol-biotin, #CMT015, HS-$(CH_2)_{10}$–CONH–$(CH_2)_3$–$(OCH_2CH_2)_3$–CH_2–NH–biotin) was obtained from Nanoscience Instrument, Inc. (USA). Alexa Fluor 647-labelled streptavidin (SA647, #S21374) was purchased from Invitrogen (Singapore).

Optical setup

As shown in Fig. 1, an attenuated total reflection (ATR) method was used for the excitation of localized and propagating surface plasmon modes on the sensor surface. A transverse magnetically (TM, p-polarization) polarized beam from a HeNe laser (λ = 632.8 nm) was coupled to a LASFN9 glass prism (n_p = 1.845) for the excitation of LSP and PSP. Onto the prism base, a glass sensor chip (n_g = 1.515) with a structure supporting surface plasmon was optically matched with matching oil (n = 1.700, Cargille Lab. NJ, USA). Aqueous samples (with a refractive index close to n_b = 1.333) were pumped at a flow rate of 0.4 mL min^{-1} through the flow-cell using a peristaltic pump. The analyzed samples circulated in the fluidic system with a total volume of 800 μL. The fluorescence light emitted from the sensor surface was collected through the flow-cell by a lens (numerical aperture NA = 0.3), passed through two band-pass filters (transmission wavelength of λ = 670 nm) and its intensity was detected by a photomultiplier tube (PMT) from Hamamatsu (H6240-01, Japan). The LASFN9 glass prism was mounted on a motorized rotation stage and angular reflectivity spectra $R(\theta)$ were recorded by using a photodiode detector and a lock-in amplifier.

Sample fabrication

Fabrication of the gold nanohole (AuNH) structures was implemented by nanoimprint lithography with a nickel mold. The nickel mold was fabricated through the electroplating and

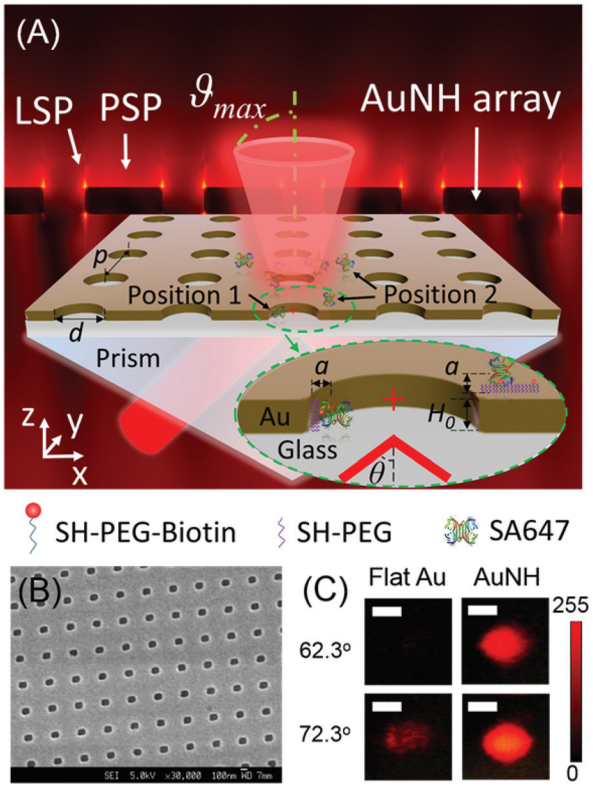

Fig. 1 (A) Scheme of the geometry used for co-excitation of PSP and LSP modes on a AuNH array for fluorescence enhancement. The cross symbol "+" indicates the position of $x = 0$, $y = 0$, $z = 0$. ϑ_{max} is the maximal angle of fluorescence emission collected through the optics. a is the average distance between the Au surface and the fluorophores. (B) SEM observation of nanohole array with a hole diameter of d = 150 nm, and pitch of p = 400 nm and metallic film thickness of H_0 = 50 nm (5 nm Cr and 45 nm Au). (C) Images of a sensing spot acquired with a CCD camera upon reflection of the excitation laser beam from a flat Au film (left) and AuNH (right) at an angle of incidence of θ = 62.3° and 72.3°, respectively. Scale bar 2 mm. The incident angle θ is the angle at the interface between the glass and the Au film.

de-molding of nickel on a silicon mold produced by E-beam lithography. The AuNH array was fabricated with a hole pitch p = 400 nm, diameter d = 150 nm, and film thickness H_0 = 50 nm (5 nm chromium and 45 nm of gold). Briefly, the AuNH array was fabricated with an electroplated nickel mold (with a nanohole structure), which was used to nanoimprint the UV curable photoresist layer (mr-UVCur21-300 nm from micro resist technology GmbH). The photoresist was then treated with reactive ion etching (RIE) to etch the indented photoresist down to the glass substrate. Afterwards, 5 nm chromium and 45 nm thick gold were deposited, and the photoresist was lifted-off by plasma etching and subsequent rinsing with acetone and isopropyl alcohol. For the flat Au film, the glass slides were cleaned in a $H_2O : NH_3 : H_2O_2$ 5 : 1 : 1 solution at 80 °C for 5 min, then rinsed with water and dried under a N_2 stream. Afterwards, the cleaned glass slides were coated with 2 nm Cr and 47 nm Au by an ultra-high vacuum thermal evaporator (Angstrom, Canada).

Surface modification

For the investigation of Alexa Fluor 647-labelled streptavidin (SA647) binding, the flat Au film and AuNH substrates were first immersed into a mixed thiol ethanol solution with 0.01 mM thiol-biotin and 0.09 mM thiol–PEG overnight. The substrates were dried under a N_2 stream before use.

Detection of SA647

The SA647 at concentrations from 0 to 10 nM in PBST buffer (PBS with 0.05% tween-20) was pumped into the flow-cell contact with biotinylated Au substrates for 20 min, followed by 5 min rinsing with PBST for each concentration of SA647.

Simulation of spectra and electromagnetic field distribution

In the simulation, three-dimensional Maxwell's equations were solved using the finite element method (COMSOL Multiphysics). The wavelength-dependent dielectric function of gold was taken from the Palik handbook. The refractive indices for air, water and glass were 1, 1.33, and 1.52, respectively. A unit cell consisting of one nanohole was simulated. At the sides of the unit cell, the Floquet periodic boundary condition was assumed in order to obtain the optical response of the whole nanohole array to a light source illuminating from an angle. An obliquely-incident linearly-polarized white light source (400–900 nm) was used. As the incident light wave strikes a metal nanohole array, its power will either be absorbed, reflected, or transmitted through the structure. The absorbed power was computed through the volume integration of the resistive heating in the gold nanoparticles, and the reflected or transmitted power was calculated through the surface integration of the far-field power flow. The sum of calculated power of absorption, reflection, and transmission is checked against the incident power to ensure the accuracy of simulation. In addition, the near-field information at the resonant wavelengths in which we are interested can be directly obtained from the simulations.

Simulations of surface plasmon-enhanced fluorescence

Besides the FEM simulations, the finite difference time domain (FDTD) method implemented in a commercially available package FDTD Solutions (Lumerical Solutions Inc., Canada) was used. Both FEM and FDTD models allow for the simulation of near field and far field characteristics of investigated plasmonic nanostructures. The comparison of results obtained by these methods allowed for checking their accuracy and validating the data. The fluorescence simulations were carried out assuming a fluorophore placed at a distance of a = 8 nm away from the AuNH and the flat Au film surface (Fig. 1A). We arrived at that distance by considering the size of the streptavidin molecule (~4–6 nm) and the length of the biotinylated PEG alkane thiol (~4.5 nm). A classical fluorescence model was used in which a fluorophore is approximated with oscillating absorption μ_{ab} and emission μ_e dipoles. In order to calculate the angular distribution of field intensity emitted by a dipole on the surface, a super-cell comprising an array of

49 × 49 periods was used. The central part including the oscillating dipole was simulated with a mesh size of 1 nm, while the rest of the supercell was simulated with a maximum mesh size of 5 nm. Total emitted power from a dipole P_{em} was calculated by the integration of the energy flux through walls of a cube closely surrounding the dipole (cube edge length of 10 nm). The quantum yield of an emitter η that is altered due to the coupling with metallic nanostructures was obtained as a ratio of the energy emitted to the far field P_r and the total emitted energy P_{em}. The energy emitted to far-field was simulated by using a two dimensional detector placed in the plane above and below the nanohole arrays. Near-field components of the electric and magnetic field intensity were recorded and transformed into the far-field dependence of P_r on the polar ϑ and azimuthal φ angles. Considering that the surface area of the nanohole wall (*i.e.* position 1) is much smaller than the gold surface at position 2, the EF was estimated only for the fluorophores located at position 2, Fig. 1A.

The excitation rate γ_e of a fluorophore that is irradiated by an incident wave at the absorption wavelength λ_{ab} was assumed as:

$$\gamma_e \propto \left|\vec{E}(\lambda_{ab})\mu_{ab}\right|^2 \quad (1)$$

which holds for small amplitude of electric field $\vec{E}(\lambda_{ab})$ when the excitation rate is far from saturation. The electric field $\vec{E}(\lambda_{ab})$ given in eqn (1) was calculated with a single unit cell and a mesh size of 1 nm. After its excitation, the fluorophore returns to its ground state by emitting a photon at a higher wavelength λ_{em} (radiative decay rate γ_r) or without emitting a photon (non-radiative decay rate γ_{nr}). An intrinsic radiative decay rate γ_r^0 and a non-radiative decay rate γ_{nr}^0 for an emitter in a homogeneous aqueous environment exhibit the quantum yield of $\eta_0 = \gamma_r^0/(\gamma_r^0 + \gamma_{nr}^0)$. When the emitter is brought in vicinity to a metallic structure, decay rates are altered leading to a change in the quantum efficiency η to:

$$\eta = \frac{\gamma_r/\gamma_r^0}{\gamma_r/\gamma_r^0 + \gamma_{abs}/\gamma_r^0 + (1-\eta^0)/\eta^0}. \quad (2)$$

In eqn (2), the term γ_r/γ_r^0 denotes the normalized radiative decay rate and γ_{abs}/γ_r^0 the additional non-radiative decay rate associated with the absorption by the metal. These ratios can be obtained from FDTD simulations as $\gamma_r/\gamma_r^0 = P_r/P_r^0$ and $\gamma_{abs}/\gamma_r^0 = (P_{em} - P_r)/P_r^0$, where P_r^0 is the power radiated to the far field by identical dipoles in homogeneous dielectric medium.

The directionality of surface plasmon-coupled emission was taken into account by using a parameter named collection efficiency CE. We assume that only light emitted at λ_{em} into a range of polar angles $\vartheta = 0 - \vartheta_{max}$ can contribute to a measurable signal in a realistic biosensor system (*e.g.*, fluorescence light is collected by a lens with a numerical aperture NA = $n\cdot\sin[\vartheta_{max}]$). As the following eqn (3) shows, the CE is defined as the emitted power that can be collected within the assumed range of polar angles which is normalized to the total power emitted to the far field:

$$CE = \int_0^{2\pi}\int_0^{\vartheta_{max}} P_r(\vartheta,\varphi)\sin\vartheta \mathrm{d}\varphi\mathrm{d}\vartheta \Big/ \int_0^{2\pi}\int_0^{\pi} P_r(\vartheta,\varphi)\sin\vartheta\mathrm{d}\varphi\mathrm{d}\vartheta \quad (3)$$

Results and discussion

The Au structure with arrays of nanoholes was designed for the amplification of fluorescence light emitted by Alexa Fluor 647 which is routinely used in fluorescence assays. This molecule absorbs light at wavelengths centred at λ_{ab} = 647 nm and emits maximum intensity of fluorescence light at a peak wavelength of λ_{em} = 670 nm. By rational design of the pitch, diameter and thickness of nanohole array arranged in a square lattice, the LSP and PSP resonances were tuned to overlap with λ_{ab} of the emitter. The diameter of the nanohole was optimized to 150 nm which provides the highest field enhancement at excitation wavelength λ_{ex} (see Fig. S1 in the ESI†).[49–51] The thickness of AuNH was set to 50 nm thereby offering efficient coupling strength to PSPs in the Kretschmann configuration, Fig. 1A. The Au structure with a nanohole diameter of 150 nm, pitch of 400 nm, and thickness of the metallic film of 50 nm (5 nm Cr and 45 nm Au) was fabricated on a BK7 glass substrate by using nanoimprint lithography, Fig. 1B. The AFM characterization of the AuNH array can be found in Fig. S2 in the ESI.†

When brought in contact with an aqueous sample, the AuNH shows two transmission peaks at 645 and 795 nm, respectively, Fig. 2A. These resonances were measured for normal incidence (θ = 0) and they qualitatively agree with the simulations which indicate that they are accompanied by a confinement of electric field intensity at nanoholes where LSP occurs. Near field simulations predict that the resonance at 645 nm is associated with the enhancement of electric field intensity at the top rim of the nanoholes that is in direct contact with the aqueous phase. The resonance at 795 nm shows the enhancement at the bottom rim of the Au nanoholes in contact with the glass substrate. The peak associated with LSPs at the top rim was further used as it allows probing an area that is better accessible to molecules diffusing from the aqueous phase above the structure. The distinct peak at λ = 500 nm is due to the interband transition of Au.[52,53]

By using the Kretschmann configuration, the excitation of LSP and PSP modes was observed by measuring reflectivity at a wavelength of λ = 632.8 nm upon tuning the incident angle θ. As shown in Fig. 2B, the excitation of PSP modes on flat Au and AuNH substrates manifests itself as a dip in reflectivity spectra at similar angles of incidence $\theta \sim 72°$, which qualitatively agrees with simulations. The overall reflectivity change of the AuNH arrays is lower than for flat Au due to the excitation of LSPs at the metallic nanoholes that are not sensitive to variation in the angle of incidence θ. Moreover, the obtained data reveal that the resonance on the AuNH array is significantly broader than for the flat Au film. This is most likely due to

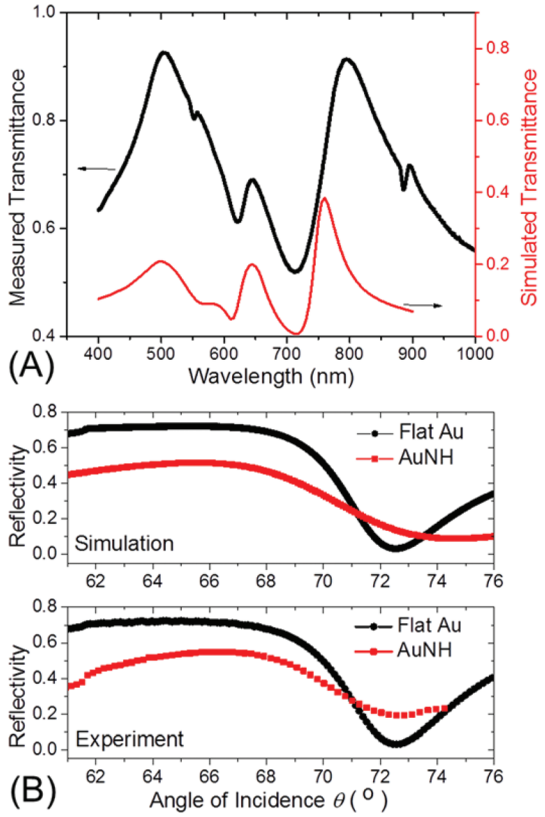

Fig. 2 (A) Experimental (black) and simulated (red) UV-vis transmission spectra of the AuNH array on a glass substrate in contact with an aqueous environment. (B) Experimental and simulated angular SPR reflectivity from flat Au and AuNH substrates at a wavelength of λ = 632.8 nm.

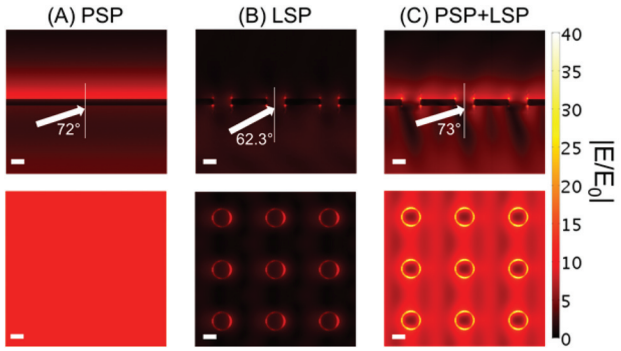

Fig. 3 Spatial distribution of electric field amplitude $|E/E_0|$ for (A) resonant excitation of PSP mode on the flat Au film, (B) LSP mode on an AuNH substrate and (C) co-excitation of LSP and PSP modes on a AuNH substrate at λ = 632.8 nm. The amplitude of the p-polarized plane wave incident at the indicated angles of incidence θ was set to 1. Scale bars are 100 nm.

radiation loss associated with the diffraction of the periodic array of nanoholes and to a change in the dispersion relation of PSP modes due to the coupling to LSPs. The difference in the coupling angle between the experiment and simulations of the AuNH sample is likely due to the roughness of the prepared structures[45] which is not taken into account in the simulations. As shown in Fig. 1C, the scattering intensity on the AuNH substrate at the angle of incidence of θ = 62.3° (off resonance) and 72.3° (at resonance) were about 10- and 3-fold higher than on the flat Au film at the corresponding angles, respectively.

Finite element method (FEM) simulations were carried out to study the near field enhancement of the electric field due to the excitation of PSP and LSP modes. Fig. 3A shows that the excitation of PSP waves at θ = 72° on a flat Au film confines the incident field perpendicular to the surface. For the AuNH array under coupling of the incident wave at θ = 62.3°, excitation occurs for LSPs located at the upper and lower rim of the Au nanoholes, Fig. 3B. When the angle of incidence increases to θ = 73°, the PSP and LSP are co-excited which leads to an increase of the field amplitude of LSP, Fig. 3C. A maximum field intensity enhancement of $|E/E_0|^2 = 1.6 \times 10^3$ is predicted at the rim of the metallic nanoholes upon co-excitation of LSP and PSP modes. This value is about an order of magnitude higher than that of the PSP mode on the flat Au film ($|E/E_0|^2$ = 130) and 8 times higher ($|E/E_0|^2 \approx 200$) than that observed for excitation of LSPs at the angle θ = 62.3°.

In order to explore details of the field enhancement upon coupling to PSP and LSP modes, a cross-section of the electric field amplitude $|E/E_0|$ in the vicinity to nanoholes was simulated as presented in Fig. 4. These plots show that field amplitude decays exponentially away from the surface for PSP excitation on the flat film, as shown in Fig. 4A. The co-excitation of PSP and LSP modes at the nanohole rim leads to about 4 times stronger field amplitude at the surface, but the field decays faster away from the surface. For instance, one can see that at distances z larger than ~40 nm from the surface, the field for co-excited LSP and PSP on the AuNH substrate is lower than the field for the PSP on the flat Au film. Furthermore, Fig. 4B displays the lateral field distribution along the y-axis for the excitation of PSPs on a flat Au film and co-excited PSP and LSP at the AuNH substrate. It indicates that the field intensity due to co-excited LSP and PSP is stronger than that occurring for the coupling to PSP only in the vicinity to the Au nanohole at a perimeter of ~100 nm away from the edge of the nanohole. At distances further away from the hole the flat surface provides stronger field enhancement.

The near field coupling of a surface plasmon-enhanced field with emitters that serve as labels in fluorescence assays was studied using the FDTD model as described in our previous work.[31] In these simulations the emitters were represented by their absorption and emission dipoles. The angular distribution of fluorescence intensity P_r (ϑ,φ) emitted into the substrate (BK7 glass) and superstrate (aqueous phase) was simulated for the randomly oriented emitters located on the flat Au and AuNH substrates. The distance between emitters and the Au surface was set to 8 nm which approximately agrees with the distance between the dye and the surface (see Fig. 1). In these simulations, we assumed that only fluorescence light emitted into aqueous medium within a cone

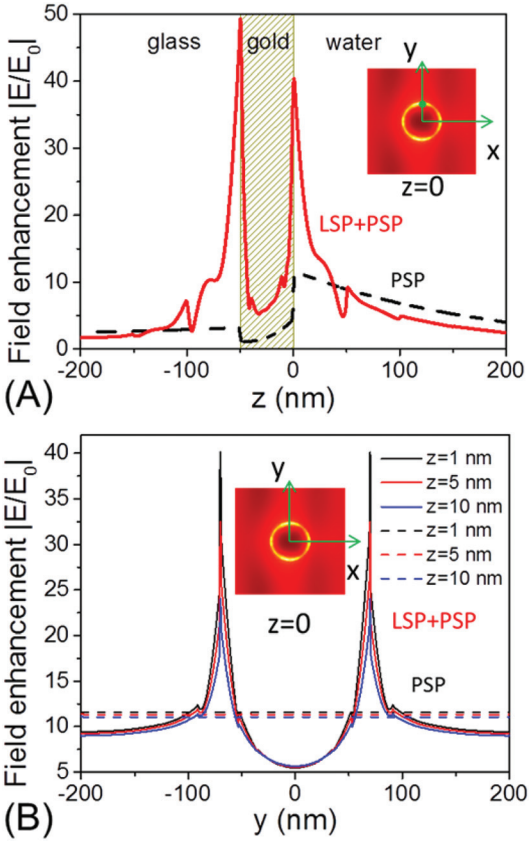

Fig. 4 (A) Comparison of cross-sections of the electric field amplitude $|E/E_0|$ as a function of distance z from the surface for the resonant excitation of PSP on a flat Au film (dashed) and co-excited LSP and PSP modes on a AuNH substrate (solid) at λ = 632.8 nm. The field distribution is plotted for x = 0 and y = 70 nm, green dot (see inset). (B) The cross-section of electric field amplitude $|E/E_0|$ as a function lateral distance along the y-axis (see inset) for different heights above the surface z = 1, 5, 10 nm for the PSP mode on the flat Au film (dashed) and the co-excited LSP and PSP modes (solid) as indicated in the inset figure x = 0.

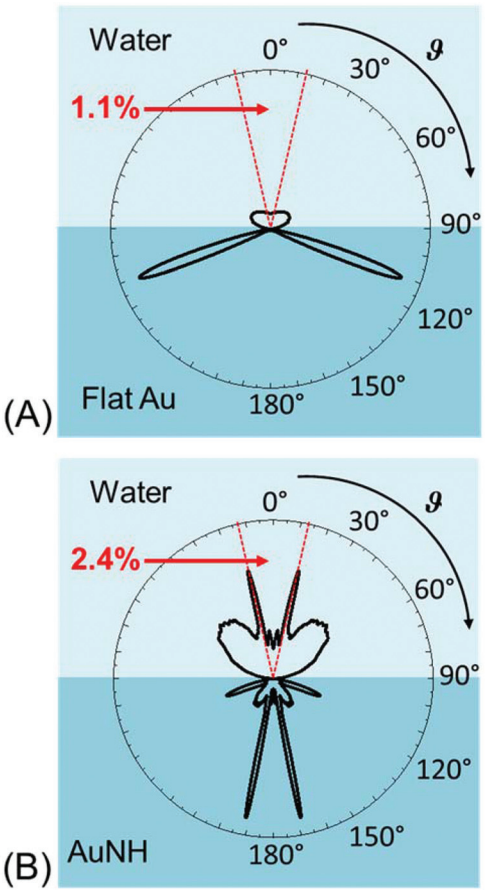

Fig. 5 Comparison of the averaged angular distribution of emitted fluorescence intensity $P_r(\vartheta, \varphi = 0)$ for emission at the wavelength of λ_{em} = 670 nm on (A) flat Au and (B) AuNH substrates. The maximum acceptance polar angles are shown as red dashed lines.

defined by the maximum polar angle ϑ_{max} = 13° contributes to the signal (corresponding to numerical aperture NA = 0.3 of the optics for collecting the emitted light).

The results presented in Fig. 5A show that for a flat Au film the majority of fluorescence light intensity is emitted into the substrate. This is mainly due to the fact that the far field emission is strongly coupled to the near field to PSPs that are subsequently out-coupled *via* a reverse Kretschmann configuration. This leads to the occurrence of highly directional lobes emitted into the substrate at a polar angle ϑ = ±110°. When introducing periodic perforation of the metallic film, diffraction provides competing means for extracting the emitted light intensity from the surface to the far field. The data in Fig. 5B reveal that the lobes associated with reverse Kretschmann outcoupling are suppressed and the emission is dominantly channeled to the far field *via* diffraction at polar angles of ϑ = ±13° into water and ϑ = ±169° onto the glass substrate. The diffraction-coupled emission in water carries the emitted energy predominantly at angles below the acceptance angle ϑ_{max}. From these data, we calculated that a fraction of photons emitted towards aqueous medium at $\vartheta < \vartheta_{max}$ (see eqn (3)) was ~2.2 times higher for the AuNH (collection efficiency, CE = 2.4%) with respect to the flat Au film (CE = 1.1%).

The model describing the interaction of the emitter with the metallic surface was used to predict the overall fluorescence intensity enhancement, that is the product defined as EF ~ $\gamma_e \times \eta \times$ CE of the enhanced excitation rate γ_e, changed quantum yield η, and collection efficiency CE for random orientation of dyes. The excitation rate γ_e is proportional to the field intensity enhancement $|E/E_0|^2$ at λ_{ex} and the collection efficiency CE quantifies the fraction of photons emitted at λ_{em} that are delivered within the cone defined by the NA (see details in the ESI†). The intrinsic quantum yield of η^0 = 0.3 was assumed according to the producer (Life Technologies) for Alexa Fluor 647 dye in water. The simulations reveal that the excitation and emission *via* co-excited PSP and LSP modes increases the fluorescence intensity F emitted within the NA by a factor of 1.5 with respect to the probing with PSP modes only. Comparing the probing by PSP and LSP (co-excited at θ = 72.3° and λ = 632.8 nm on AuNH) and by PSP (excited at θ = 72.3° and λ = 632.8 nm on flat Au film) with that for the

Table 1 Fluorescence enhancement EF on flat Au and AuNH substrates at different angles of incidence, normalized to the value obtained off resonance at 62.3° for the flat Au

	Flat Au (72.3°)	AuNH (62.3°)	AuNH (72.3°)
Simulation	47	4.7	72
Experiment	33.3	8.3	100

probing at the off-resonance regime (excited at θ = 62.3° and λ = 632.8 nm on the flat Au film), the fluorescence enhancement by a factor of 72 and 47, respectively, is predicted by the simulations, as shown in Table 1.

In order to experimentally evaluate the potential of co-excited LSPs and PSPs for the amplification of fluorescence assay, we prepared substrates with flat Au and AuNH and modified them with a thiol self-assembled monolayer (SAM) containing terminal biotin groups (see Fig. 1). These substrates were used for the excitation of either solely PSP or co-excited LSP and PSP modes for probing of affinity binding of streptavidin that was labelled by Alexa Fluor 647 dye. The angular SPR reflectivity and fluorescence spectra measured for the flat Au film after binding of SA647 at the concentrations from 10 pM to 10 nM show that the fluorescence intensity F increases at the resonant angle θ = 72.3° from 4×10^3 to 3.5×10^5 cps, Fig. 6A. However, on the AuNH array the affinity binding of SA647 results in a 2–3 times stronger fluorescence signal (from 8×10^3 to 1.2×10^6 cps), Fig. 6B.

The fluorescence kinetic measurement at the resonant angle also indicated 2–3 times higher fluorescence intensity changes on AuNH substrates upon the binding of SA647 with respect to the flat Au film, Fig. 6C. The fluorescence intensity is saturated after incubating SA647 at a concentration higher than 10 nM, which is not the case for the reflectivity measurement. This is due to the high fluorescence intensity which exceeds the linear range and approaches the maximum detectable intensity (3.6×10^6 cps) of the photomultiplier. The calibration curves for the affinity binding of SA647 on flat Au and AuNH substrates at on-resonant and off-resonant angles are shown in Fig. 6D. The limit of detection (LOD) for the detection of SA647 is determined as the concentration of SA647 at which the response is 3 times the standard deviation of fluorescence fluctuation. The highest sensitivity was achieved on AuNH at an on-resonant angle (*i.e.* upon co-excitation of LSP and PSP) with LOD of 0.7 pM, which is about 2 times and 14 times better than that for the PSP enhanced fluorescence and

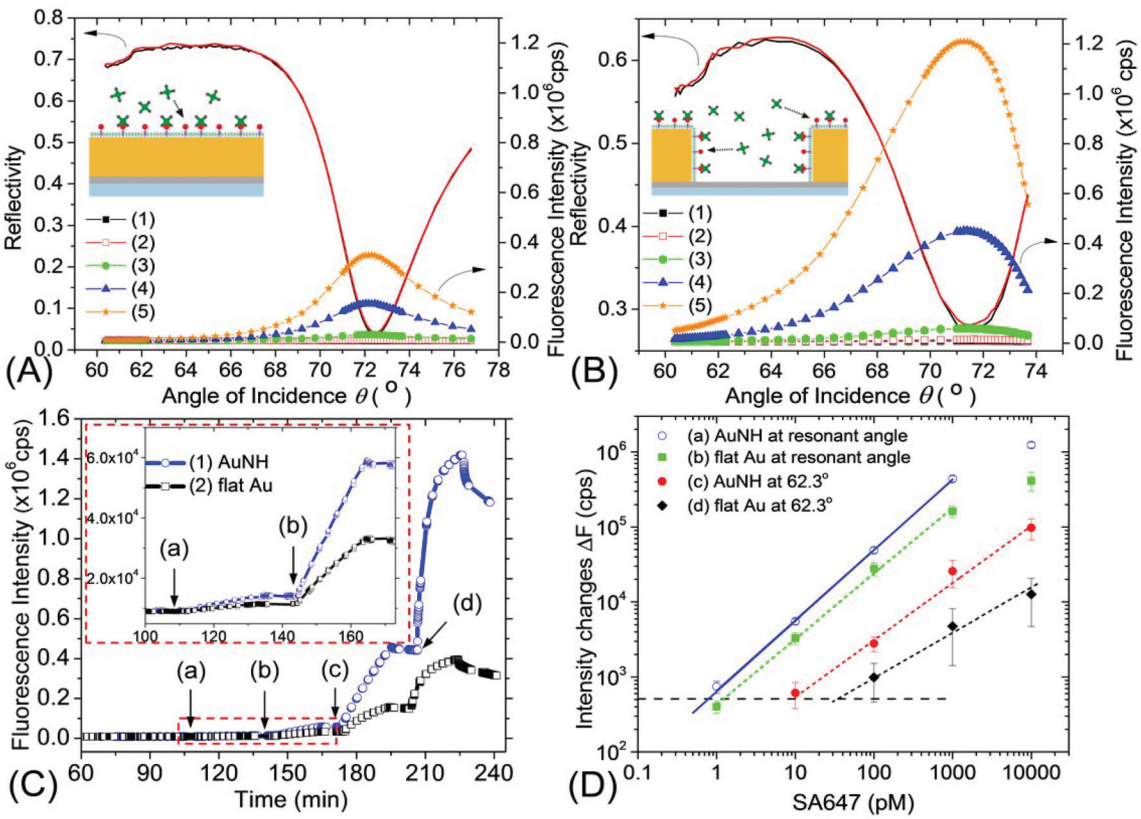

Fig. 6 The angular SPR reflectivity (solid lines) and fluorescence spectra (line with symbols) measured on (A) flat Au and (B) AuNH substrates upon the affinity binding of SA647 at concentrations of (1) 0, (2) 10 pM, (3) 100 pM, (4) 1 nM and (5) 10 nM. (C) The kinetics of the fluorescence signal on (**1**) AuNH and (**2**) flat Au films upon the sequential binding of SA647 from solutions with a concentration of (a) 10 pM, (b) 100 pM, (c) 1 nM and (d) 10 nM. (D) The fluorescence intensity changes as a function of SA647 concentration on (a, c) an AuNH array and (b, d) a flat Au film at incident angles of 72.3° and 62.3°, respectively.

LSP enhanced fluorescence, respectively. Even though the LSP excited at 62.3° shows the maximum intensity enhancement up to $|E_{sp}/E_0|^2$ = 200 fold, Fig. 3B, which is higher than that of PSP, the LSP enhanced fluorescence shows about 7-fold lower sensitivity, Fig. 6D. This is because of the small sensing volume on the AuNH located at the rim of the nanohole.

The experimental and simulated EF on the flat Au film and the AuNH substrate are normalized to the flat Au film at an off-resonance angle (62.3°) and summarized in Table 1. The experimental results on the AuNH substrate show higher EF than expected from the simulations. Note that in the simulation, the molecules located on the wall of the nanoholes were not considered because the wall area is very small in comparison with the overall surface area. In addition, the molecules were assumed to distribute homogeneously on the metallic surface.

One may argue that the larger surface area of the AuNH with respect to the flat Au film contributes the fluorescence enhancement. Essentially, the surface area of the AuNH substrate can be estimated as $S_{hole} = n(p^2 - \pi R^2 + 2\pi R H_0)$, where R and n are the radius and the number the nanoholes, respectively. p is the pitch of the nanohole array, and H_0 is the thickness of the Au film (see Fig. 1). For the same size of the flat Au film, the surface area is $S_{flat} = np^2$. Accordingly, the surface area of AuNH is about 1.04 times higher than the Au film. This 4% surface enlargement is too small to explain the 3 times higher fluorescence enhancement on AuNH as compared with the flat Au film. The number of streptavidins bound on the AuNH was assumed to be the same as that on the flat Au film, which was estimated to equal 7 to 696 molecules per 400 × 400 nm^2, after 20 min incubation of 1 pM to 100 pM, respectively, based on fitting the kinetic curves (see Fig. S4†). The fluorescence enhanced sensitivity on co-excited LSP and PSP modes is about $G = 4.88 \times 10^{-6}$ cps per molecule, which is about 3.2 times higher than the PSP enhanced fluorescence (see the ESI†).

Conclusion

In summary, the co-excitation of LSP and PSP significantly enhances the field intensity which allows for improved fluorescence enhancement when compared to geometries where only individual PSP or LSP modes interact with an emitter. The performed simulations indicate that maximum field enhancement occurs at edges of the nanoholes where emitters are preferentially excited at their absorption wavelength. In addition, a highly directional surface plasmon-coupled fluorescence beam with an emission wavelength can be observed on the AuNH substrate which allows for more efficient extraction of fluorescence light from the sensor surface. The fluorescence measurement upon the binding of Alexa Fluor 647-labelled streptavidin on the AuNH substrate revealed a fluorescence enhancement of about 10^2 as compared to a reference flat Au surface irradiated off-resonance. The fluorescence enhancement can be further improved by the selective modification of the nanohole array to allow the molecular binding only on "hotspots" such as the edge of the nanohole.[54,55] We anticipate that this method benefits from both the advantages of the stronger electromagnetic field of LSP and the longer penetration depth (higher probing volume) of PSP, as well as the high directional fluorescence emission for ultrasensitive sensing applications. The co-excitation of LSP and PSP has also indicated feasibility for the enhancement of label-free sensors upon detection of biomolecules by monitoring the resonant wavelength shift.[56] In addition, the presented structure for directional surface plasmon-enhanced fluorescence detection can be implemented to a sensor substrate with an open, flow-through, nanohole array design.[57] This design was shown to provide means for more efficient collection of the target analyte on the sensor surface that is not hindered by slow diffusion.[58]

Acknowledgements

The authors thank the financial support from the Science & Engineering Research Council (SERC) of the Agency for Science, Technology and Research (A*STAR), for projects under the numbers 102 152 0014 and 102 152 0015. In addition, this work was partially supported by the Austrian NANO Initiative (FFG and BMVIT) through the NILPlasmonics project within the NILAustria cluster (http://www.NILAustria.at) and by Austrian Science Fund (FWF) project ACTIPLAS (P244920-N20).

Notes and references

1 J. Homola, *Chem. Rev.*, 2008, **108**, 462–493.
2 J. N. Anker, W. P. Hall, O. Lyandres, N. C. Shah, J. Zhao and R. P. Van Duyne, *Nat. Mater.*, 2008, **7**, 442–453.
3 S. Linic, P. Christopher and D. B. Ingram, *Nat. Mater.*, 2011, **10**, 911–921.
4 S. C. Warren and E. Thimsen, *Energy Environ. Sci.*, 2012, **5**, 5133–5146.
5 S. Mukherjee, F. Libisch, N. Large, O. Neumann, L. V. Brown, J. Cheng, J. B. Lassiter, E. A. Carter, P. Nordlander and N. J. Halas, *Nano Lett.*, 2013, **13**, 240–247.
6 F. Pincella, K. Isozaki and K. Miki, *Light: Sci. Appl.*, 2014, **3**, e133.
7 M. W. Knight, H. Sobhani, P. Nordlander and N. J. Halas, *Science*, 2011, **332**, 702–704.
8 W. S. Cai, A. P. Vasudev and M. L. Brongersma, *Science*, 2011, **333**, 1720–1723.
9 Q. Q. Gan, F. J. Bartoli and Z. H. Kafafi, *Adv. Mater.*, 2013, **25**, 2385–2396.
10 N. Liu, F. F. Wen, Y. Zhao, Y. M. Wang, P. Nordlander, N. J. Halas and A. Alu, *Nano Lett.*, 2013, **13**, 142–147.
11 N. P. W. Pieczonka and R. F. Aroca, *Chem. Soc. Rev.*, 2008, **37**, 946–954.
12 J. R. Lombardi and R. L. Birke, *Acc. Chem. Res.*, 2009, **42**, 734–742.

13 T. Neumann, M. L. Johansson, D. Kambhampati and W. Knoll, *Adv. Funct. Mater.*, 2002, **12**, 575–586.
14 J. R. Lakowicz, K. Ray, M. Chowdhury, H. Szmacinski, Y. Fu, J. Zhang and K. Nowaczyk, *Analyst*, 2008, **133**, 1308–1346.
15 M. Bauch, K. Toma, M. Toma, Q. W. Zhang and J. Dostalek, *Plasmonics*, 2014, **9**, 781–799.
16 H. Aouani, O. Mahboub, N. Bonod, E. Devaux, E. Popov, H. Rigneault, T. W. Ebbesen and J. Wenger, *Nano Lett.*, 2011, **11**, 637–644.
17 S. D. Choudhury, R. Badugu and J. R. Lakowicz, *Acc. Chem. Res.*, 2015, **48**, 2171–2180.
18 J. Malicka, I. Gryczynski, Z. Gryczynski and J. R. Lakowicz, *Anal. Chem.*, 2003, **75**, 6629–6633.
19 I. Gryczynski, J. Malicka, Z. Gryczynski and J. R. Lakowicz, *J. Phys. Chem. B*, 2004, **108**, 12568–12574.
20 H. Aouani, O. Mahboub, E. Devaux, H. Rigneault, T. W. Ebbesen and J. Wenger, *Nano Lett.*, 2011, **11**, 2400–2406.
21 T. Ming, L. Zhao, H. J. Chen, K. C. Woo, J. F. Wang and H. Q. Lin, *Nano Lett.*, 2011, **11**, 2296–2303.
22 A. G. Curto, G. Volpe, T. H. Taminiau, M. P. Kreuzer, R. Quidant and N. F. van Hulst, *Science*, 2010, **329**, 930–933.
23 T. H. Taminiau, F. D. Stefani, F. B. Segerink and N. F. Van Hulst, *Nat. Photonics*, 2008, **2**, 234–237.
24 G. M. Akselrod, C. Argyropoulos, T. B. Hoang, C. Ciraci, C. Fang, J. N. Huang, D. R. Smith and M. H. Mikkelsen, *Nat. Photonics*, 2014, **8**, 835–840.
25 A. G. Brolo, S. C. Kwok, M. G. Moffitt, R. Gordon, J. Riordon and K. L. Kavanagh, *J. Am. Chem. Soc.*, 2005, **127**, 14936–14941.
26 X. Q. Cui, K. Tawa, K. Kintaka and J. Nishii, *Adv. Funct. Mater.*, 2010, **20**, 945–950.
27 M. J. Levene, J. Korlach, S. W. Turner, M. Foquet, H. G. Craighead and W. W. Webb, *Science*, 2003, **299**, 682–686.
28 P. F. Guo, S. Wu, Q. J. Ren, J. Lu, Z. H. Chen, S. J. Xiao and Y. Y. Zhu, *J. Phys. Chem. Lett.*, 2010, **1**, 315–318.
29 Y. Fu, J. Zhang and J. R. Lakowicz, *J. Am. Chem. Soc.*, 2010, **132**, 5540–5541.
30 S. Khatua, P. M. R. Paulo, H. F. Yuan, A. Gupta, P. Zijlstra and M. Orrit, *ACS Nano*, 2014, **8**, 4440–4449.
31 M. Bauch and J. Dostalek, *Opt. Express*, 2013, **21**, 20470–20483.
32 R. Bardhan, N. K. Grady, J. R. Cole, A. Joshi and N. J. Halas, *ACS Nano*, 2009, **3**, 744–752.
33 K. Sugawa, T. Tamura, H. Tahara, D. Yamaguchi, T. Akiyama, J. Otsuki, Y. Kusaka, N. Fukuda and H. Ushijima, *ACS Nano*, 2013, **7**, 9997–10010.
34 G. P. Acuna, F. M. Moller, P. Holzmeister, S. Beater, B. Lalkens and P. Tinnefeld, *Science*, 2012, **338**, 506–510.
35 D. Punj, M. Mivelle, S. B. Moparthi, T. S. van Zanten, H. Rigneault, N. F. van Hulst, M. F. Garcia-Parajo and J. Wenger, *Nat. Nanotechnol.*, 2013, **8**, 512–516.
36 A. Kinkhabwala, Z. F. Yu, S. H. Fan, Y. Avlasevich, K. Mullen and W. E. Moerner, *Nat. Photonics*, 2009, **3**, 654–657.
37 J. R. Lakowicz, *Plasmonics*, 2006, **1**, 5–33.
38 F. Yu, B. Persson, S. Lofas and W. Knoll, *Anal. Chem.*, 2004, **76**, 6765–6770.
39 D. F. Yao, F. Yu, J. Y. Kim, J. Scholz, P. E. Nielsen, E. K. Sinner and W. Knoll, *Nucleic Acids Res.*, 2004, **32**, e177.
40 Y. Wang, J. Dostalek and W. Knoll, *Biosens. Bioelectron.*, 2009, **24**, 2264–2267.
41 A. Kasry and W. Knoll, *Appl. Phys. Lett.*, 2006, **89**, 101106.
42 J. Dostalek, A. Kasry and W. Knoll, *Plasmonics*, 2007, **2**, 97–106.
43 Y. Wang, A. Brunsen, U. Jonas, J. Dostalek and W. Knoll, *Anal. Chem.*, 2009, **81**, 9625–9632.
44 M. Tabatabaei, M. Najiminaini, K. Davieau, B. Kaminska, M. R. Singh, J. J. L. Carson and F. Lagugné-Labarthet, *ACS Photonics*, 2015, **2**, 752–759.
45 F. Yu, S. Ahl, A. M. Caminade, J. P. Majoral, W. Knoll and J. Erlebacher, *Anal. Chem.*, 2006, **78**, 7346–7350.
46 X. N. Wang, Y. Y. Wang, M. Cong, H. B. Li, Y. J. Gu, J. R. Lombardi, S. P. Xu and W. Q. Xu, *Small*, 2013, **9**, 1895–1899.
47 Y. Liu, S. P. Xu, H. B. Li, X. G. Jian and W. Q. Xu, *Chem. Commun.*, 2011, **47**, 3784–3786.
48 M. Schmelzeisen, Y. Zhao, M. Klapper, K. Mullen and M. Kreiter, *ACS Nano*, 2010, **4**, 3309–3317.
49 Y. Wang, L. Wu, X. Zhou, T. I. Wong, J. Zhang, P. Bai, E. P. Li and B. Liedberg, *Sens. Actuators, B*, 2013, **186**, 205–211.
50 L. Wu, P. Bai and E. P. Li, *J. Opt. Soc. Am. B*, 2012, **29**, 521–528.
51 J. Zhang, Y. Wang, T. I. Wong, X. Liu, X. Zhou and B. Liedberg, *Nanoscale*, 2015, **7**, 17244–17248.
52 K. L. Shuford, M. A. Ratner, S. K. Gray and G. C. Schatz, *Appl. Phys. B: Lasers Opt.*, 2006, **84**, 11–18.
53 H. W. Gao, J. Henzie and T. W. Odom, *Nano Lett.*, 2006, **6**, 2104–2108.
54 L. Feuz, M. P. Jonsson and F. Hook, *Nano Lett.*, 2012, **12**, 873–879.
55 L. Feuz, P. Jonsson, M. P. Jonsson and F. Hook, *ACS Nano*, 2010, **4**, 2167–2177.
56 L. S. Live, A. Dhawan, K. F. Gibson, H. P. Poirier-Richard, D. Graham, M. Canva, T. Vo-Dinh and J. F. Masson, *Anal. Bioanal. Chem.*, 2012, **404**, 2859–2868.
57 N. Sharma, H. Keshmiri, X. D. Zhou, T. I. Wong, C. Petri, U. Jonas, B. Liedberg and J. Dostalek, *J. Phys. Chem. C*, 2016, **120**, 561–568.
58 C. Escobedo, A. G. Brolo, R. Gordon and D. Sinton, *Anal. Chem.*, 2010, **82**, 10015–10020.